The FEBS Journal

FEBS PRESS science publishing by scientists

Crystal structure of NirF: insights into its role in heme d_1 biosynthesis

Thomas Klünemann[1], Manfred Nimtz[2], Lothar Jänsch[2], Gunhild Layer[3] and Wulf Blankenfeldt[1,4]

1 Structure and Function of Proteins, Helmholtz Centre for Infection Research, Braunschweig, Germany
2 Cellular Proteome Research, Helmholtz Centre for Infection Research, Braunschweig, Germany
3 Institute of Pharmaceutical Sciences, Pharmaceutical Biology, Albert-Ludwigs-Universität Freiburg, Germany
4 Institute for Biochemistry, Biotechnology and Bioinformatics, Technische Universität Braunschweig, Germany

Keywords
denitrification; heme d_1; NirF; tetrapyrrole biosynthesis; X-ray structure

Correspondence
W. Blankenfeldt, Structure and Function of Proteins, Helmholtz Centre for Infection Research, Inhoffenstrasse 7, 38124 Braunschweig, Germany
Tel: +49 531 6181-7000
E-mail: wulf.blankenfeldt@helmholtz-hzi.de

(Received 13 January 2020, revised 17 March 2020, accepted 31 March 2020)

doi:10.1111/febs.15323

Certain facultative anaerobes such as the opportunistic human pathogen *Pseudomonas aeruginosa* can respire on nitrate, a process generally known as denitrification. This enables denitrifying bacteria to survive in anoxic environments and contributes, for example, to the formation of biofilm, hence increasing difficulties in eradicating *P. aeruginosa* infections. A central step in denitrification is the reduction of nitrite to nitric oxide by nitrite reductase NirS, an enzyme that requires the unique cofactor heme d_1. While heme d_1 biosynthesis is mostly understood, the role of the essential periplasmatic protein NirF in this pathway remains unclear. Here, we have determined crystal structures of NirF and its complex with dihydroheme d_1, the last intermediate of heme d_1 biosynthesis. We found that NirF forms a bottom-to-bottom β-propeller homodimer and confirmed this by multi-angle light and small-angle X-ray scattering. The N termini are adjacent to each other and project away from the core structure, which hints at simultaneous membrane anchoring via both N termini. Further, the complex with dihydroheme d_1 allowed us to probe the importance of specific residues in the vicinity of the ligand binding site, revealing residues not required for binding or stability of NirF but essential for denitrification in experiments with complemented mutants of a Δ*nirF* strain of *P. aeruginosa*. Together, these data suggest that NirF possesses a yet unknown enzymatic activity and is not simply a binding protein of heme d_1 derivatives.

Database
Structural data are available in PDB database under the accession numbers 6TV2 and 6TV9.

Introduction

Denitrification, the respiration on nitrate and nitrite, is a facultative trait that enables some bacterial species to proliferate under anaerobic conditions [1]. Denitrification consists of a four-step reductive process, starting from nitrate and leading via nitrite to nitric oxide (NO), nitrous oxide (N_2O), and finally to dinitrogen. Denitrifying bacteria are employed to remove *N*-oxyanions from wastewater; however, they compete with plants for nutrients in agriculture and even affect the climate, as the gaseous intermediates are active greenhouse gases [1]. Furthermore, denitrification also plays a role in infectious disease as exemplified by the

Abbreviations
dd1, dihydroheme d_1; DDSH, 12,18-didecarboxysiroheme; LB, lysogeny broth; MALS, multi-angle light scattering; MBP, maltose-binding protein; *P.*, *Pseudomonas*; PEG, polyethylene glycol; R_g, radius of gyration; SAM, *S*-adenosyl methionine; SAXS, small-angle X-ray scattering; SEC, size-exclusion chromatography; SUMO, small ubiquitin-related modifier; tNCS, translational noncrystallographic symmetry.

opportunistic human pathogen *Pseudomonas aeruginosa*, which resorts to denitrification to support its proliferation in regions depleted of oxygen by the host's immune system [2].

During denitrification in *P. aeruginosa*, the reduction of nitrite to nitric oxide is catalyzed by the cytochrome cd_1 nitrite reductase NirS [3,4]. This homodimeric enzyme contains an N-terminal cytochrome *c* domain with a covalently attached heme *c* that serves as an electron entry point and a C-terminal eight-bladed β-propeller domain that noncovalently binds heme d_1 to function as the active site during nitrite reduction [5]. While the catalytic mechanism of NirS is well understood, some aspects in the biosynthesis of its cofactor heme d_1 are still unclear [4,6].

Heme d_1 is an isobacteriochlorin and features two carbonyl groups at rings A and B as well as an acrylate moiety at ring D [7,8]. The *nir*-operon of denitrifying bacteria encodes most of the enzymes necessary for heme d_1 biosynthesis, starting from the common tetrapyrrole precursor uroporphyrinogen III [9-12]. The first steps of heme d_1 biosynthesis are the conversion of uroporphyrinogen III to 12,18-didecarboxysiroheme (DDSH) via precorrin-2, sirohydrochlorin, and siroheme, successively catalyzed by NirE, CysG (in some organisms), and NirDLGH (Fig. 1) [13-16]. The intermediate DDSH is further converted by the radical *S*-adenosyl methionine (SAM) enzyme NirJ, which sequentially removes the propionate groups from pyrrole rings A and B [17]. Based on mass spectrometry, a tetrapyrrole with two γ-lactones involving the acetate groups at C2 and C7 has been observed as the final product of this reaction, but these lactones may be artifacts of the extraction procedure and alternatives such as hydroxyl groups or hydrogen replacing the propionate chains were proposed [17]. Importantly, the generation of dihydro-heme d_1 (dd1), the last intermediate of heme d_1 biosynthesis and substrate of the oxidoreductase NirN, was not observed in experiments with NirJ, suggesting that dd1 may be produced by NirF, the only remaining less well-characterized protein encoded in the *nir*-operon [17,18].

While its exact role still remains unclear, previous work highlighted that NirF is an essential component of the heme d_1 biosynthesis pathway [9,19-21]. It resides in the periplasm of heme d_1-producing bacteria, where it is even membrane-anchored in some species including *P. aeruginosa*, and this localization was found to be required *in vivo* [21,22]. It has been demonstrated by UV/Vis spectroscopy that NirF can bind both oxidized and reduced heme d_1 as well as dd1 [18,21]. Exchange of His41 in *Paracoccus pantotrophus* NirF abolished heme d_1 binding, and it was proposed that this residue acts as a proximal iron ligand [21]. Similar to NirN and NirS, NirF is predicted to contain an eight-bladed β-propeller, albeit without being extended by a cytochrome *c* domain. Interestingly, *in vivo* cross-linking experiments in *P. aeruginosa* identified NirN and NirS as transient interaction partners of NirF, hinting at potential substrate shuttling between these proteins [22]. Further, NirF seems to be part of a larger protein complex involved in denitrification, as it was also isolated together with nitric oxide reductase (NorB and NorC) and the electron transfer protein NosR after *in vivo* cross-linking [23]. Together, these data indicate that NirF is an important component of the denitrification process, most likely acting downstream of NirJ and upstream of NirN. To gain further insights into its role, we have determined crystal structures of NirF from *P. aeruginosa* with and without bound dd1 and used these structures to design mutagenesis experiments that highlight the importance of residues in the vicinity of the dd1 rings A and B for the function of the enzyme. Our experiments render further support to the hypothesis that NirF acts on the product of NirJ and provides dd1 to NirN.

Results and Discussion

Protein production, purification, and crystallization

Heterologous production of *P. aeruginosa* NirF in *Escherichia coli* was established with a construct that lacked the signal sequence for the export into the periplasm and the cysteine residue necessary for membrane attachment via a lipid anchor. By adding N-terminal solubility tags such as small ubiquitin-related modifier (SUMO) or maltose-binding protein (MBP), the amount of recombinant protein could be enhanced up to > 500 $mg \cdot L^{-1}$ culture. Interestingly, the solubility of purified NirF after tag removal was highly temperature-dependent: When a NirF solution at 8 $mg \cdot mL^{-1}$ was stored overnight at 4 °C, most of the protein precipitated, whereas it was stable when stored at room temperature. Crystallization by the sitting-drop vapor diffusion method yielded crystals belonging to the $P2_1$ space group containing eight molecules in the asymmetric unit, but analysis with XTRIAGE [24] revealed severe anisotropy and a large off-origin peak in the Patterson map, indicating the presence of translational noncrystallographic symmetry (tNCS; Table 1). Diffraction data were therefore treated anisotropically using the STARANISO server [25], giving resolution cutoffs of 1.7 Å, 1.6 Å, and 2.1 Å along the axes of

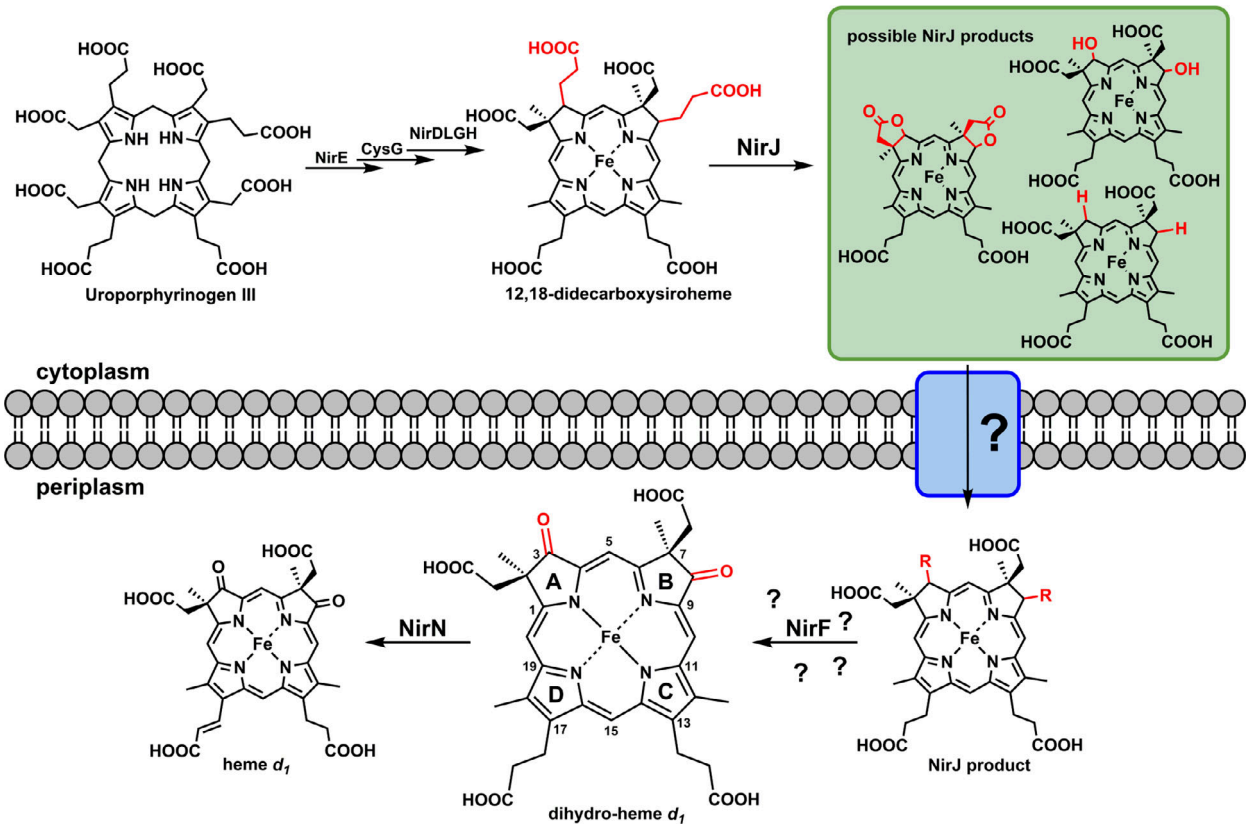

Fig. 1. Graphical representation of the heme d_1 biosynthesis pathway based on a review by Bali *et al.* [11] with consideration of more recent work [17,18]. The figure was generated with ChemDraw 18.2 and shows the stepwise biosynthesis of heme d_1 starting from the heme precursor uroporphyrinogen III, which is first methylated, dehydrogenated, ferrochelated, and decarboxylated by NirE, CysG, and NirDLGH, respectively, followed by the removal of the propionate groups by NirJ. The product of NirJ has not been identified unambiguously; therefore, possible products are depicted. Following the transport into the periplasm via an unknown mechanism, the product of NirJ may be taken up by NirF to be converted to dd1 before being oxidized to heme d_1 by NirN.

the fitted ellipsoid. Despite the presence of tNCS, initial phasing was achieved by molecular replacement with an ensemble of the d1-domain of NirN and NirS (for details, see the Materials and methods section). The refinement converged with a model that contains all except the six N-terminal residues and had *R*-values of R_{work} = 16.3% and R_{free} = 20.4%.

Overall structure

NirF folds as an eight-bladed β-propeller with four antiparallel β-strands per blade and a counterclockwise propagation when viewed from the top (Fig. 2). The first blade consists of the three N-terminal and one C-terminal strands and, thus, represents the closing point of this circular protein. This topology allows a C-terminal η-helix to partially close the bottom of the propeller. All other blades propagate from the inside to the outside. Overall, the structure of NirF is highly similar to the d1-domains reported for NirS and NirN, resulting in low RMSDs of 2.4 Å and 2.1 Å, respectively [5,26].

Analyzing the structure with PISA [27] revealed that NirF has an interface to form homodimers, in which the bottoms of two β-propellers are attached to each other, albeit with low stabilization by solvation free energy ($\Delta^i G$ = −4 kcal·mol^{-1}). The two monomers are rotated relative to each other such that the first blade of one propeller is approximately placed between the second and the third of the other (Fig. 2, topology diagram). Closer inspection of the interface reveals a crescent-shaped hydrophobic patch that is probably responsible for the negative $\Delta^i G$ values. In addition, the four dimers contained in the asymmetric unit are on average stabilized by 15 hydrogen bonds and 22 salt bridges. Of the residues involved in these interactions, R331 seems especially important since it is deeply buried in a negative pocket of the second monomer. β-propeller proteins

Table 1. Data collection and refinement statistics.

	MALX-E-NirF	NirF	NirF dd1
Data collection statistics			
Resolution shell type	Spherical	Ellipsoidal	Ellipsoidal
Wavelength (Å)	1.0000	1.0000	1.7365
Space group	P 1 2_1 1	P 1 2_1 1	P 1 2_1 1
Unit cell dimensions			
a, *b*, *c* (Å)	76.09, 117.60, 103.31	101.3, 147.83, 108.72	101.20, 149.44, 110.17
α, β, γ (°)	90, 90.175, 90	90, 98.21, 90	90, 98.48, 90
Resolution range (Å)[a]	117.6–4.0 (4.47–4.00)	107.60–1.56 (1.73–1.56)	100.09–1.89 (2.14–1.89)
Ellipsoidal resolution (Å; direction)[h]	–	1.70 (0.930*a** + 0.367*c**) 1.56 (*b**) 2.11 (−0.41*a** * 0.912*c**)	2.10 (0.955*a** − 0.296*c**) 1.89 (*b**) 2.76 (0.13*a** + 0.992*c**)
Total no. of reflections[a]	63 534 (17 507)	1 073 574 (54 339)	918 555 (24 628)
No. of unique reflections[a]	15 238 (4329)	289 596 (14 420)	149 789 (7472)
Multiplicity[a]	4.2 (4.0)	3.7 (3.8)	6.1 (3.3)
Completeness (%; spherical)[a]	98.9 (98.9)	65.2 (69.2)	58.8 (9.9)
Completeness (%; ellipsoidal)[a,h]	–	94.7 (69.3)	93.0 (52.6)
$R_{p.i.m}$ (all *I*+&*I*−)[a,b]	0.467 (0.728)	0.067 (0.394)	0.076 (0.342)
$I/\sigma(I)$[a]	2.9 (1.8)	6.4 (1.7)	6.1 (1.9)
$CC_{1/2}$[a,c]	0.255 (0.182)	0.995 (0.655)	0.991 (0.742)
Largest Patterson peak with length larger than 15 Å (tNCS)			
Fractional coordinates[i]	–	0.5, 0.276, 0.5	0.5, 0.285, 0.5
Height relative to origin (%)[i]	–	38.529	41.565
Refinement statistics			
No. of reflections used in refinement[a]	–	289 582 (2508)	149 796 (623)
No. of reflections used for R_{free}[a]	–	14 291 (117)	7422 (37)
R_{work}[a,d]	–	0.1628 (0.2472)	0.2153 (0.3085)
R_{free}[a,e]	–	0.2024 (0.2989)	0.2576 (0.3155)
No. of protein residues	–	2976	2976
No. of nonhydrogen atoms	–	27 416	25 402
Protein	–	23 789	23 477
Ligand	–	58	392
Solvent	–	3569	1533
Average *B*-factor (Å^2)[g]	–	20.8	22.9
Protein	–	19.1	22.7
Water	–	41.6	21.1
Ligands	–	31.4	25.3
RMSD[g]	–		
Bond length (Å)	–	0.006	0.010
Bond angle (°)	–	0.87	1.09
Ramachandran plot (%)[g]	–		
Favored regions	–	98.38	97.13
Allowed regions	–	1.62	2.87
Outliers	–	0.00	0.00
Rotamer outliers (%)	–	0.20	0.36
Cis-prolines (%)		10.13	10.13
Clash score[f]	–	3.31	2.65
MolProbity score[f]	–	1.05	1.17
PDB Code		6TV2	6TV9

[a]Values in parentheses are for the highest resolution shell; [b]$R_{p.i.m} = \Sigma_{hkl}\{1/[N(hkl) - 1]\}^{1/2} \times \Sigma_i|I_i(hkl) - \langle I(hkl)\rangle|/\Sigma_{hkl}\ \Sigma_i\ I_i(hkl)$; [c]CC1/2 = $\Sigma(x - \langle x\rangle)(y - \langle x\rangle)/[\Sigma(x - \langle x\rangle)2\Sigma(y - \langle y\rangle)2]1/2$; [d]$R_{work} = (\Sigma_{hkl}||F_{obs}| - k|F_{calc}||)/(\Sigma_{hkl}|F_{obs}|)$; [e]$R_{free}$ is the same as R_{work} with 5% of reflections chosen at random and omitted from refinement; [f]Statistics calculated with the MolProbity web server [56] (http://molprobity.biochem.duke.edu/); [g]Statistics calculated with Table 1 tool of PHENIX suite [50]); [h]Statistics calculated with STARANSIO server [25]; [i]Calculated with XTRIAGE [24].

commonly interact by their sides to extend their β-sheets, as, for example, in the d1-domains of NirS [5,28]. It is possible that the unusual dimerization allows NirF to form side-by-side heterooligomers with the β-propellers of NirN and NirS, which are known transient interaction partners of NirF [22].

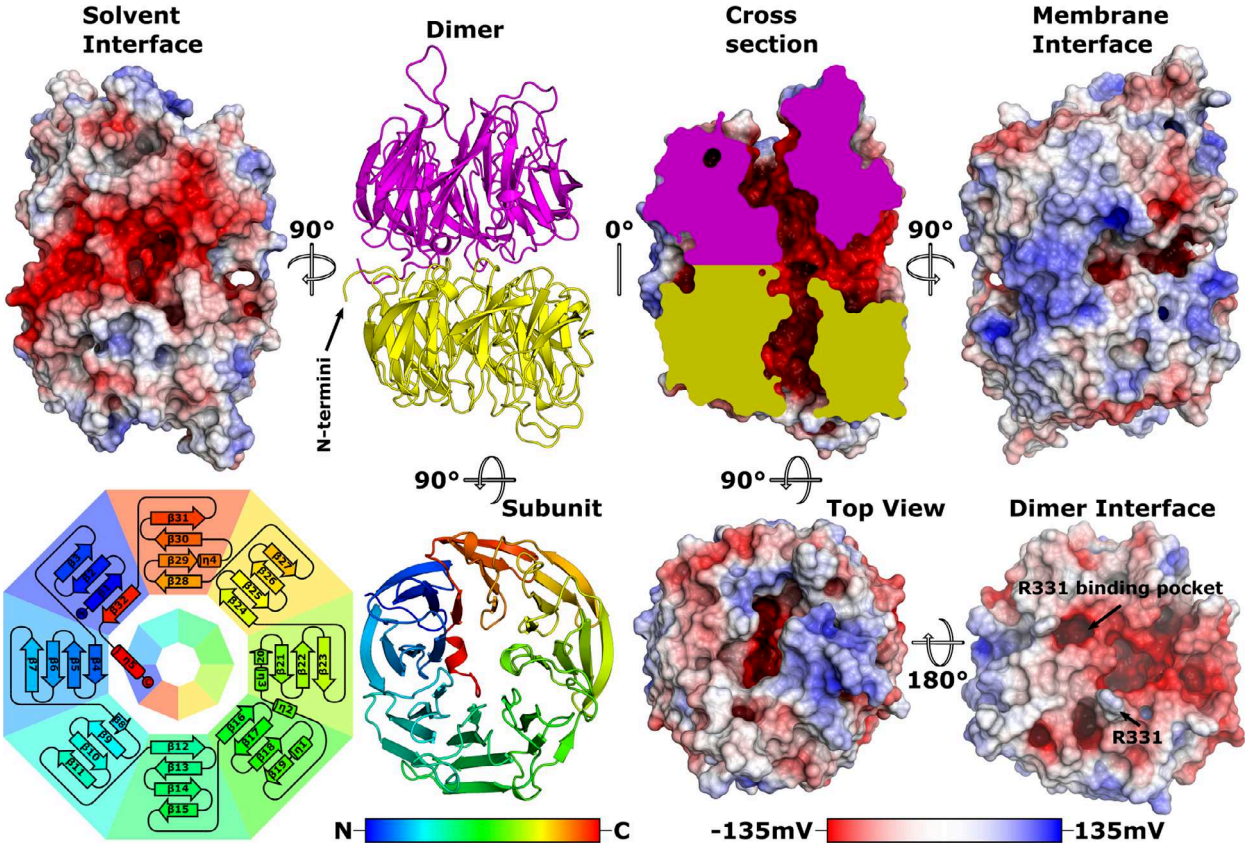

Fig. 2. Structure of NirF from *Pseudomonas aeruginosa* depicted as a C_α cartoon or as a surface model. The surface is colored with a red-white-blue gradient representing the surface potential as calculated by APBS [57] to highlight the different charge distribution associated with the orientation toward the membrane (positive) and toward the solvent (negative), as well as the negatively charged T-shaped tunnel. In addition, the position of R331, a residue that interlocks the protomers of the dimer, has been highlighted. The subunits of the dimer are shown in yellow and magenta. Note that the dimerization mode enables simultaneous membrane anchoring via both N termini, since these are located on the same side of NirF dimer. Rainbow coloration represents the propagation of the chain from N to C terminus. The inner ring of the topology diagram represents the relative orientation of the second monomer. The same color scheme is used throughout. Depictions have been generated with the PYMOL molecular graphics system (Schrödinger LLC, New York, NY, USA; version 2.3.2).

To confirm the bottom-to-bottom homodimeric assembly of NirF, we measured small-angle X-ray scattering (SAXS) curves. The resulting *ab initio* bead model calculated from these data is consistent with the NirF dimer shown in Fig. 3. Further, theoretical scattering curves and radii of gyration (*R*g) derived from other dimer and monomer models of NirF fit the measured data less well, lending additional support to the relevance of the dimer observed *in crystallo*.

An important consequence of the observed dimerization is that the C terminus must have a defined length, since elongation would interfere with dimerization or tetrapyrrole binding (as shown later). This may explain why the NirF variant from *P. pantotrophus*, which was produced with a C-terminal purification tag, was reported to be monomeric and why a *P. aeruginosa* mutant strain lacking NirF but producing a recombinant, C-terminally tagged variant of NirF displayed attenuated growth under denitrifying conditions [21,22]. Further, twenty-one aligned sequences of NirF from different organisms all end at the same position and with a hydrophobic amino acid (Fig. 4), indicating that dimerization might be a common feature of NirF.

As NirF of *P. aeruginosa* was found to be membrane-anchored through its N terminus [22], it is interesting to note that both N termini are positioned next to each other in the dimer, enabling simultaneous membrane anchoring (Fig. 2). The surface facing the membrane possesses an overall positive charge, which seems to enable interactions with phospholipids. In contrast, the solvent-exposed side and even more so the interior of the d_1-domains exhibit a mostly negative character. Surprisingly, the insides of both monomers are connected via a narrow T-shaped tunnel that

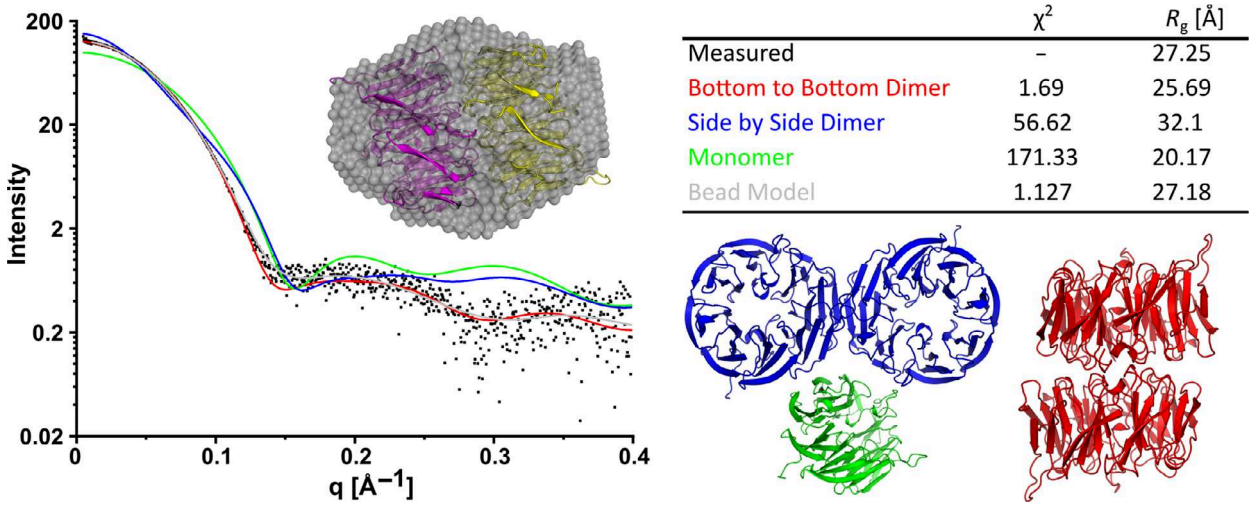

	χ^2	R_g [Å]
Measured	–	27.25
Bottom to Bottom Dimer	1.69	25.69
Side by Side Dimer	56.62	32.1
Monomer	171.33	20.17
Bead Model	1.127	27.18

Fig. 3. Solution SAXS of NirF of *Pseudomonas aeruginosa*. Measured data are represented as black dots. Colored solid lines represent theoretical scattering curves derived from the models shown on the right. FOXS [55] or Dammin [54] was used for the calculation, chi-square values represent goodness of fit to measured data, and R_g represents the derived radius of gyration. This measurement shows that NirF is a bottom-to-bottom homodimer in solution. The figure has been generated with the PYMOL molecular graphics system (Schrödinger LLC, version 2.3.2).

has an additional exit toward the solvent-exposed side. Using MOLEONLINE 2.0 [29], the radius of the bottleneck of this tunnel was determined to be 2 Å, which is too narrow to allow for the passage of tetrapyrroles. Therefore, the tunnel likely represents a channel that allows water or similarly sized molecules to access the tetrapyrrole binding site (next paragraph).

Dihydro-heme d_1 binding site

Crystals of NirF were soaked with dd1 to gain a detailed insight into tetrapyrrole binding. Well-defined $|F_OF_C|$ difference electron density with anomalous difference density at the expected position of the iron atom allowed placing dd1 (Fig. 5). The model was refined at 2.1, 1.9, and 2.7 Å along the axes of the fitted ellipsoid and gave R-values of R_{work} = 21.5% and R_{free} = 25.8%. Occupancies of the ligand bound to the eight chains contained in the asymmetric unit refined to values between 75% and 100% (details in the Materials and methods section). Not surprisingly, dd1 is bound in the middle of the d1-domain, similar to other d1-type hemes in NirN and NirS, despite being slightly tilted in the binding pocket [5,26] (Figs 5 and 6). The propionate groups at rings C and D of the tetrapyrrole are deeply buried in the negatively charged binding pocket. A positive surface patch accommodates the acetate groups of rings A and B. Interestingly, the propionate moiety of ring D is oriented toward the propionate moiety of ring C. This may lead to a discrimination between dd1 and heme d_1, since the latter carries an acrylate side chain at the D-ring that tends to adopt a planar conformation with respect to the tetrapyrrole ring system, allowing electron delocalization through the π-orbital system as, for example, seen in the structure of NirS [5]. In NirF, such a conformation would lead to clashes with H325.

Closer inspection reveals that upon binding of dd1, H48 and H238 rotate to ligate the central iron of the tetrapyrrole (Fig. 5). Hydrophobic interaction partners of dd1 are I90, V280, F281, L324, and F368. E240 reorients to avoid clashes with the incoming dd1 and interacts with the propionate of ring C via a water molecule. In addition, the propionate moiety interacts with several water molecules located in the T-shaped tunnel mentioned above, which, for example, establishes a bridge to R372. Therefore, the T-shaped tunnel may allow proton exchange reactions at the buried propionate moieties of dd1 even after it has bound to NirF. The acetate groups of rings A and B of dd1 form hydrogen bonds with R21 and R65 and, again through bridging water molecules, with R340 and H48. S50 and D185 are found in the vicinity of dd1, but do not seem to contact the ligand. Surprisingly, neither direct nor indirect interactions with the oxo groups of dd1 are present in the final model, even though these positions may ultimately be affected by the unknown function of NirF. A comparison of 21 NirF sequences (seven of each class of α-, β-, and γ-proteobacteria) shows that, except for E240 and V280,

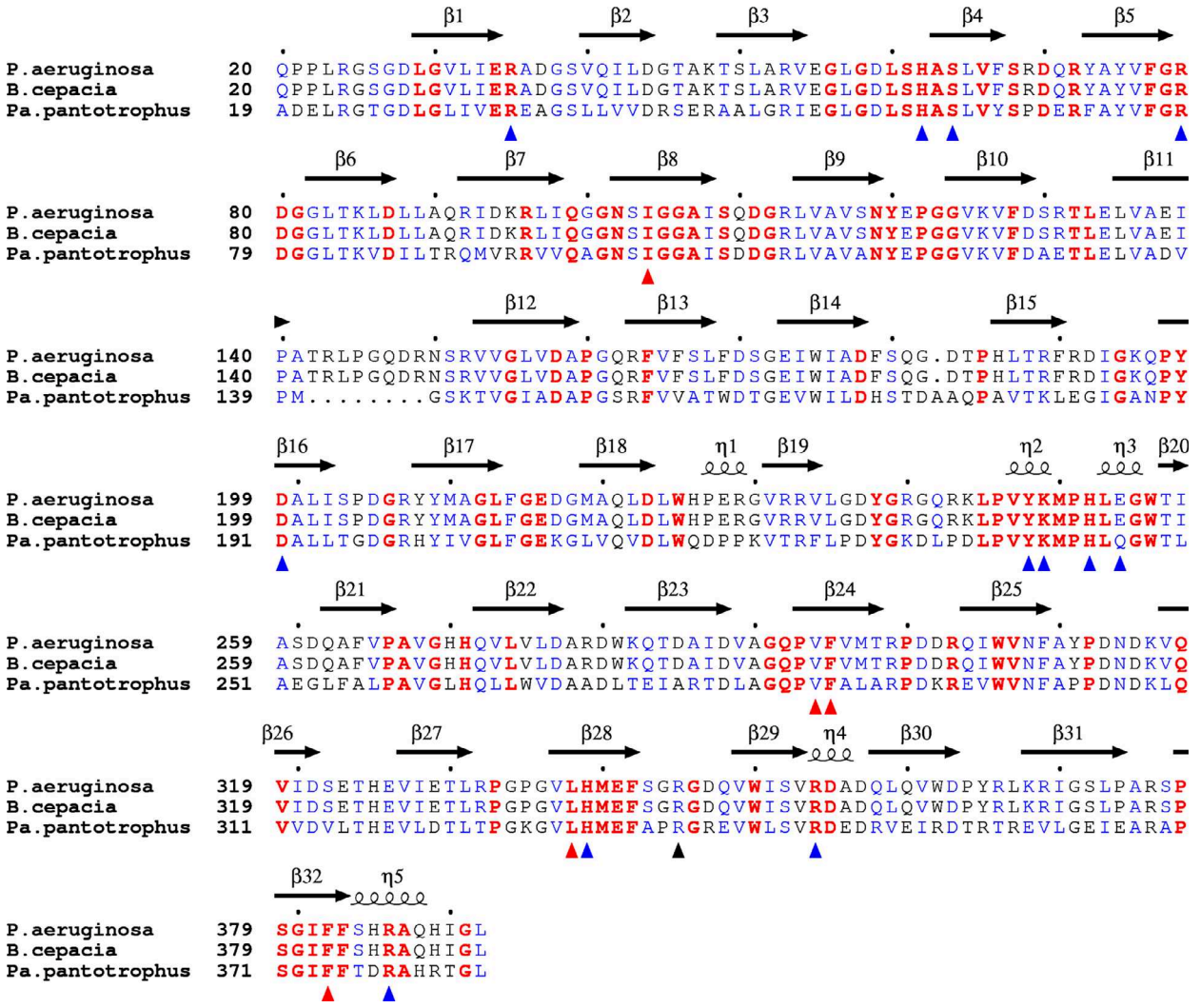

Fig. 4. Sequences of NirF from 21 organisms (seven of each σ-, β-, or γ-proteobacteria) aligned with CLUSTALω [58] and depicted with ESPRIPT3.0 [59]. Only one representative sequence for each division is depicted. Numbering of sequences is based on complete sequences including the signal peptide. Red bold letters mark identity in all sequences and blue a 70% conservation as calculated with the Risler matrix. Secondary structure elements of NirF without bound dd1 are depicted on top of the sequences. Blue arrows on the bottom mark residues mutated in this study, red arrows indicate hydrophobic residues that interact with dd1, and a black arrow highlights R331 as a conserved residue of the dimer interface. The complete sequence alignment is provided in a separate file. The following NCBI sequence accession codes point to the sequences that have been used to compile the complete alignment: EEA94743.1; AEK99469.1; GEK68819.1; TYC79074.1; WP_012179837.1; AEI95091.1; BBJ05361.1; CCK76408.1; SPC20826.1; SCU75091.1; EHF12350.1; BAD11782.1; AEV63752.1; AAZ43107.1; CEF26833.1; ADB24715.1; CDK98612.1; ASJ24358.1; GAO23490.1; SMB28481.1; KIF81953.1.

all of the mentioned residues are identical (Fig. 4). V280 is sometimes found as an isoleucine, whereas E240 is commonly found as a glutamine or an arginine. This implies that E240 probably is not important for the activity of NirF.

Comparison to NirN and NirS

As mentioned above, an eight-bladed β-propeller that binds d1-type hemes is also found in the dehydrogenase NirN and in the nitrite reductase NirS [5,26]. The unknown but essential role of NirF must differ from these proteins, suggesting that dd1-binding residues that are different from those found in NirN or NirS are involved in its function (Figs 6 and 7). The dd1 iron-ligating distal H48 and proximal H238 are conserved in all three proteins; however, the proximal histidine of NirS does not coordinate the iron directly, but rather is involved in substrate (nitrite) binding. The hydrophobic nature of V280, F281,

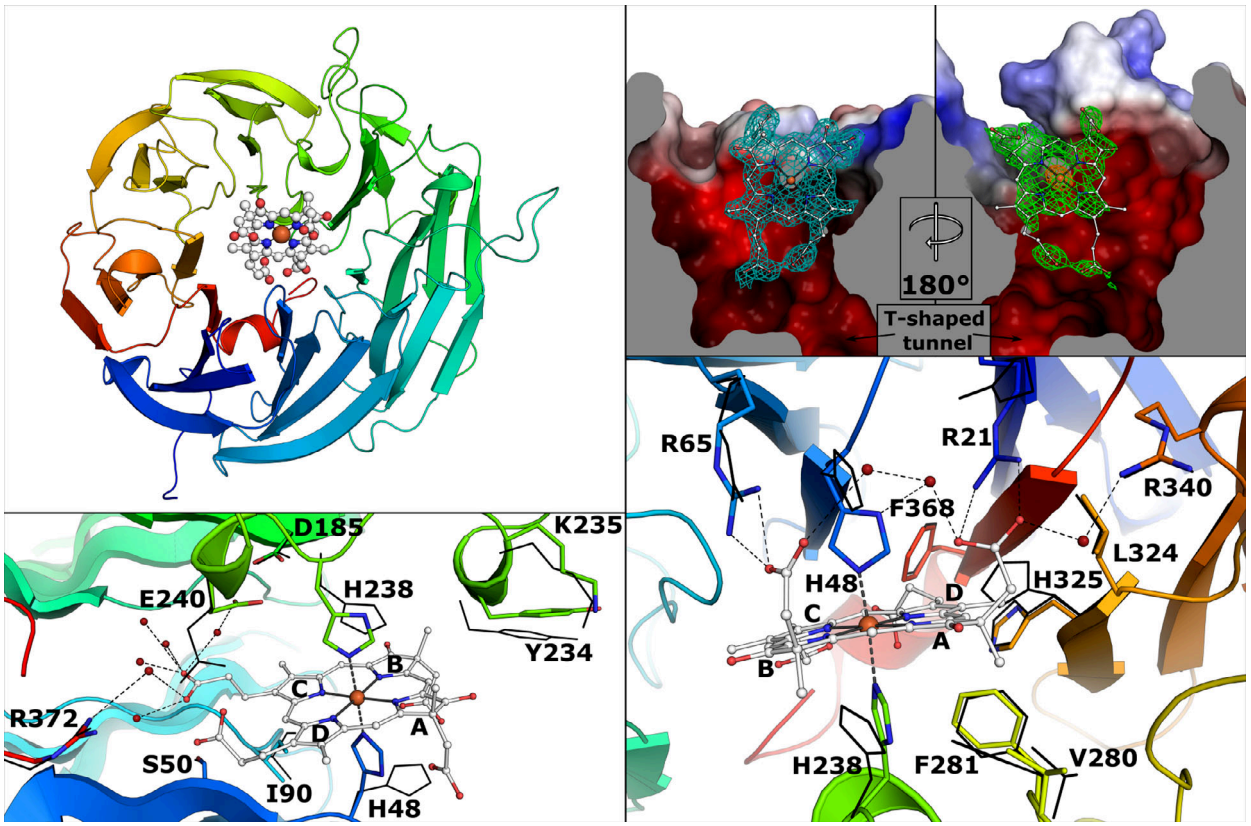

Fig. 5. Depiction of the dd1 binding side. The backbone is shown as a cartoon model, residues as sticks, dd1 as white ball-and-stick model, and water molecules as red spheres. Positions of residues without bound dd1 are depicted as black lines. Thin dashed black lines represent H-bonds. The cyan mesh represents the final $2F_oF_C$ map at a σ-level of 1, the green mesh depicts the F_oF_c map prior to first placement of a dd1 molecule at a σ-level of 3, and the orange mesh presents the anomalous map at a σ-level of 15. Depictions have been generated with the PYMOL molecular graphics system (Schrödinger LLC, version 2.3.2).

L324, and F368 is conserved across the three proteins, whereas the equivalent position of I90 is found as an arginine that interacts with the oxo or acetate groups of the B-ring in NirN and NirS. Interestingly, the acetate groups of rings A and B of dd1 interact with three arginines in all three proteins, which, with the exception of R65, originate from different positions of the β-propeller. This makes the NirF-specific R340 an interesting candidate for further investigation. Other residues that are unique to NirF are S50, E240, and R372. Another overall unique feature of NirF is the loop that connects β-sheets five and six (residues 226–236, loop 1), which is more extended than in NirN and NirS and places Y234 as well as K235 nearly on top of dd1, implying functional involvement of these NirF-conserved residues. Loop 2 (residues 126–139), connecting β-sheets three and four, adopts a different conformation in all three proteins. As this loop is involved in dimerization in NirS, it might fulfill a similar interfacing function in the previously detected transient heterooligomers of NirF with NirN or NirS [22]. We have therefore devised experiments to probe the importance of these amino acids, also including D185, since this residue of the tetrapyrrole binding site is conserved across all three β-propeller proteins but has not been analyzed to date.

Impact of amino acid exchanges in NirF on denitrification by *Pseudomonas aeruginosa*

Because the function of NirF is not known yet, we used the crystal structure in complex with dd1 to design variants of the protein and assess their effect on the denitrification capacity of *P. aeruginosa* to gain new insight into the role of this protein. Toward this, we employed the *P. aeruginosa* PA01 Δ*nirF* strain RM301 [9] carrying plasmids encoding versions of NirF in which residues in the vicinity of the ligand binding site had been replaced by alanine. For these newly generated *P. aeruginosa* strains, growth curves were measured under denitrifying conditions. Additionally, the nitrate consumption and the accumulation

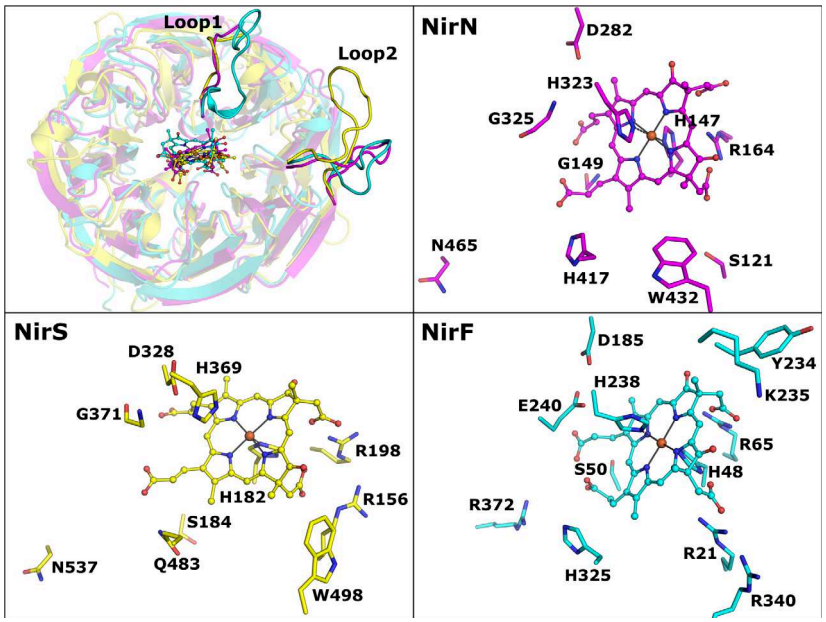

Fig. 6. Comparison of d1-domain of NirF (cyan), NirN (magenta), and NirS (yellow) after superposition. Panel 1 shows the overall similarity of the domains and highlights the differences of loops 1 and 2 as well as the relatively tilted binding mode of dd1 in NirF. The other panels show positions of residues in the dd1 binding pocket from the same viewpoint. Depictions have been generated with the PYMOL molecular graphics system (Schrödinger LLC, version 2.3.2).

of nitrite in the medium were determined. This system was already employed to confirm the location of NirF in the periplasm in earlier work [22]. As shown in Fig. 8 and as reported previously [9,22], *P. aeruginosa* strain RM301 indeed displayed impaired growth under denitrifying conditions, whereas the strain RM301 that produced wild-type NirF from a plasmid even outgrew the parental strain.

The complementation of strain RM301 with NirF variants carrying exchanges of S50, Y234, E240, H324, and R340 against alanine had no influence on the growth of the respective strain, suggesting that these residues are not required for the activity of NirF. Exchange of R21 or R372, on the other hand, led to attenuated growth but without accumulation of nitrite, hinting at a probably reduced level of active nitrite reductase NirS, and hence impaired heme d_1 production. Surprisingly, growth was not only inhibited after exchange of the iron-ligating histidines H48 and H328, but also when the propionate group-coordinating R65 and K235 were replaced by alanine. Finally, exchange of D185 also led to impaired growth, albeit some residual NirS activity seemed to be present.

Impact of amino acid exchanges on the biophysical properties of NirF

Because the impaired growth of *P. aeruginosa* RM301 producing altered versions of NirF could be rooted in inherent instability of the respective protein variant, we also produced and purified the recombinant proteins and tested for their thermal stability as well as dimerization and dd1 binding (Figs 9 and 10). All of the NirF variants, with exception of the D185A amino acid exchange, could be purified with the procedure established for the wild-type protein. The D185A NirF, however, precipitated within minutes after the addition of SUMO-protease to remove the SUMO solubility tag, and only small amounts of the protein could be recovered and purified. Interestingly, the melting point of the purified protein was only 3.1 K lower than that of the wild-type protein, which is considerably less than the 13.4 K lower melting temperature for R372A NirF, a variant that could be produced without difficulties. In addition, the D185A variant bound dd1 with similar efficiency as the wild-type protein. Together with the observation that denitrification was still active in the respective *P. aeruginosa* strain, this indicates that exchange of D185 impairs the folding but not the stability of the protein and that this residue is probably also not involved in the activity of NirF.

The large decrease in the melting point of the R372A variant without significantly compromising growth under denitrifying conditions prompted us to analyze this variant further. Interestingly, the R372A protein eluted later in size-exclusion chromatography (SEC) and showed a molecular weight corresponding to a NirF monomer in multi-angle light scattering (MALS) measurements. Although R372 is not involved in the dimer interface, it might stabilize the C-terminal η-helix on which it resides. Changes within this helix are expected to interfere with dimerization, and our findings indicate that this dimerization

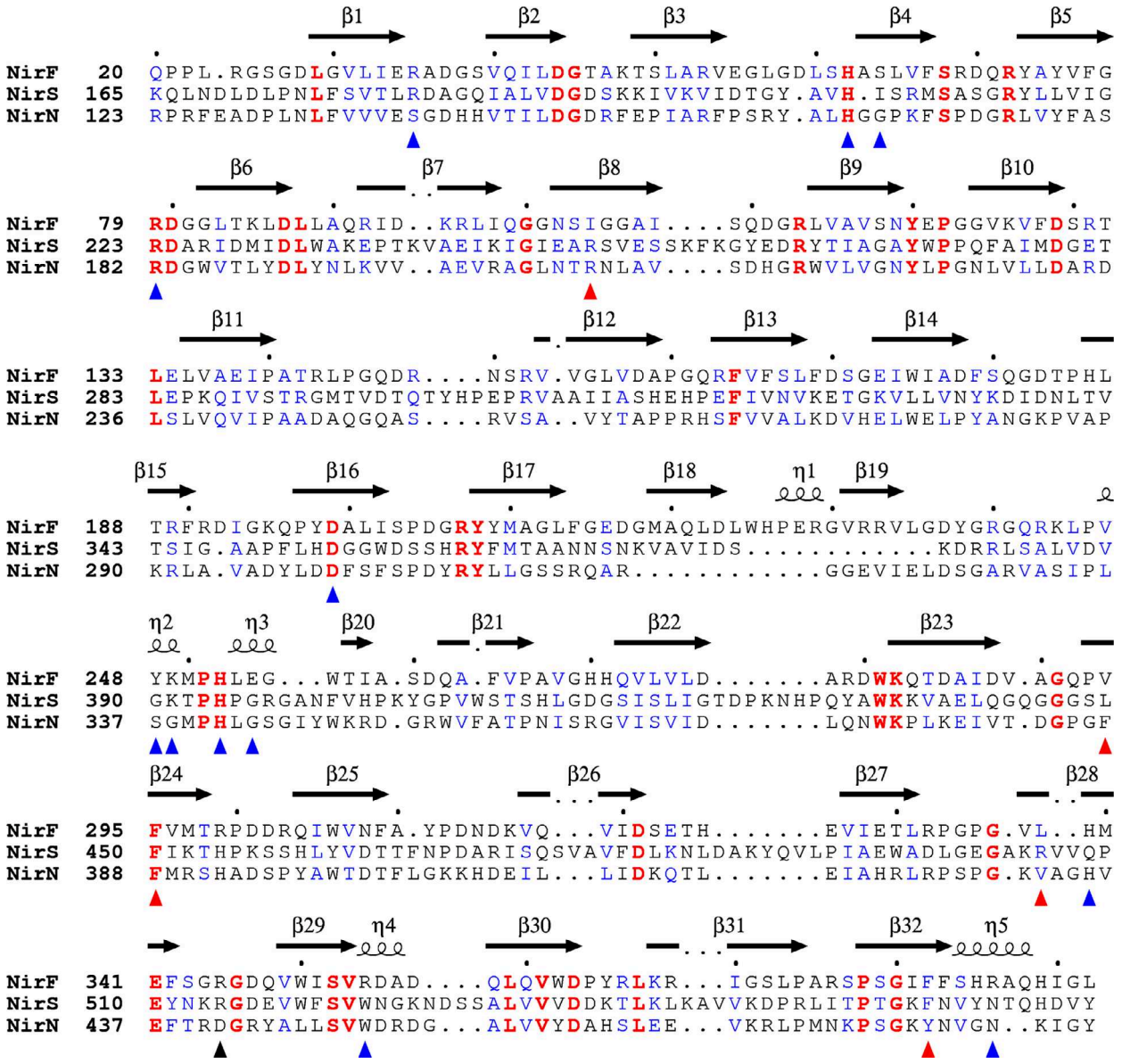

Fig. 7. Sequences of the d1-domain of NirF, NirS, and NirN from *Pseudomonas aeruginosa* aligned with CLUSTALω [58] and depicted with ESPRIPT3.0 [59]. The same symbols as in Fig. 4 have been used. NCBI sequence accession codes are as follows: EHF12350.1, NirF; BAA12683.1, NirN; and AAG03908.1, NirS.

stabilizes the protein without having considerable functional importance, a well-known behavior for many homodimeric proteins [30].

The binding of dd1 to NirF was investigated by UV/Vis absorption spectroscopy after mixing the protein and the tetrapyrrole (Fig. 10). While the isolated dd1 exhibits characteristic absorption maxima at 410 nm (Soret band) and 683 nm, the binding of the tetrapyrrole to wild-type NirF leads to a split Soret band with maxima at 393 and 420 nm as well as a shift of the 683 nm feature to 612 nm. Additionally, dd1 binding to NirF was also assessed by testing for co-elution from a size-exclusion column (Fig. 10). Both methods demonstrated that the exchange of histidines H48 and H238, which coordinate the central iron atom of dd1, completely abolished tetrapyrrole binding. Exchange of arginines R21, R65, and R372 resulted in reduced dd1 binding, whereas replacement of D185 and K235 surprisingly increased it. Together, these experiments hint at important functional roles for R65 and K235, since the respective NirF variants are stable and

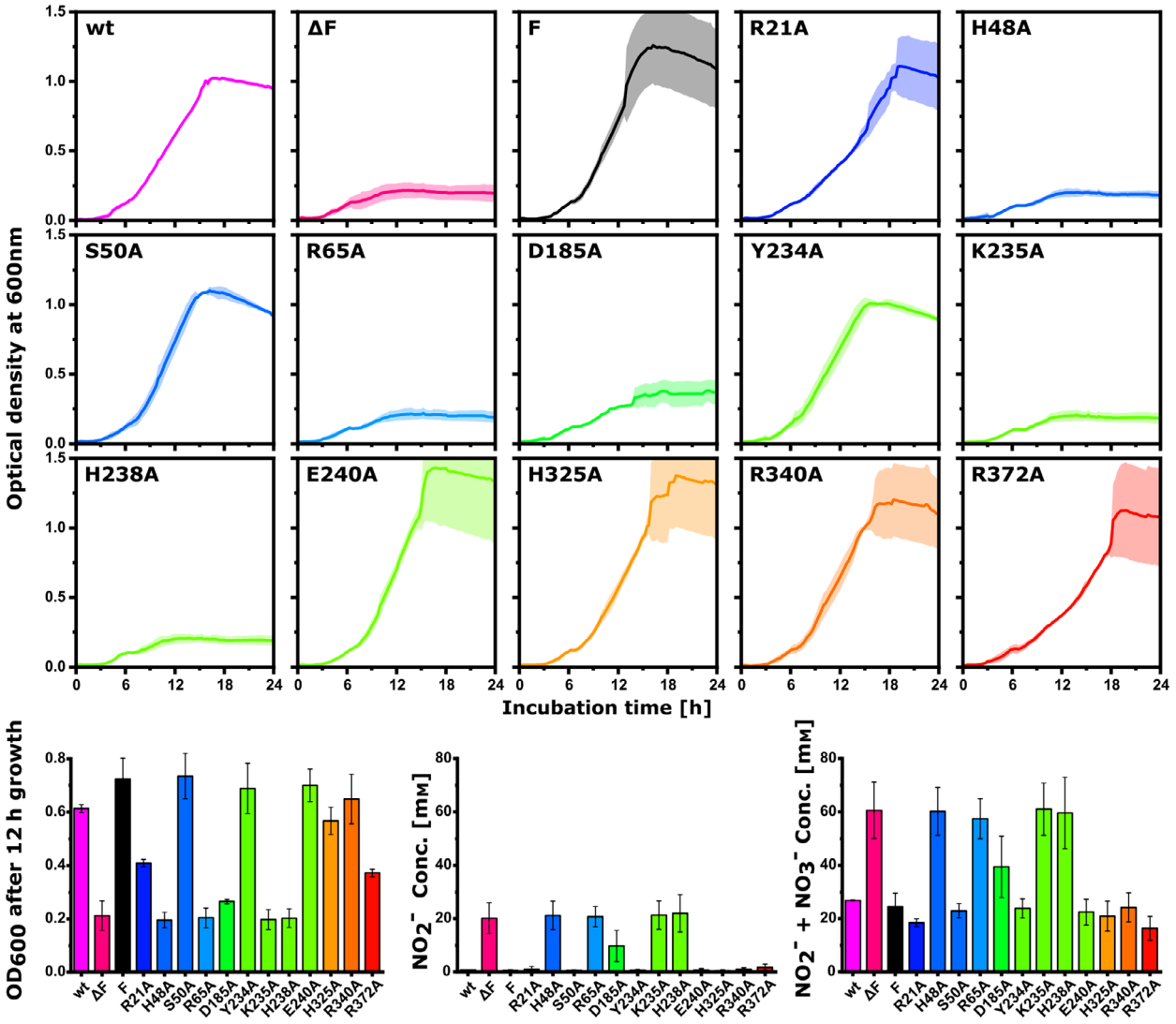

Fig. 8. Averaged growth curves of two replicates of wild-type *Pseudomonas aeruginosa* PAO1 and of four biological replicates of the *P. aeruginosa* PAO1 strain RM301 complemented with plasmid-borne NirF containing different amino acid exchanges. Errors (SD, $n = 4$) are marked as pale broadened lines. Large errors toward the end of the experiment are due to the occurrence of nitrogen gas bubbles, confirming denitrification activity in the culture. Samples marked as wt or ΔF are wild-type PAO1 or strain RM301 containing only the plasmid backbone, respectively. F designates strain RM301 containing a plasmid with unmutated *nirF*. Bar graphs depict the OD_{600} after 12 h taken from the growth curves for easy comparison, and the media concentration of NO_2^- and NO_3^- after 24 h of incubation with standard deviation error bars ($n = 4$). The coloration correlates to residue positions in the sequence as shown in Fig. 5.

bind dd1 *in vitro*, but are not able to complement the *P. aeruginosa* RM301 strain *in vivo*.

Implications for the role of NirF in heme d_1 biosynthesis

The identification of NirF variants that bind the heme d_1 precursor dd1 but are inactive *in vivo* together with the observation that dd1 is relatively solvent-exposed, and its A- and B-rings point outwards in the NirF complex lead us to speculate about two alternative roles of the protein in heme d_1 biosynthesis. First, as has been suggested previously, NirF might be responsible for the uptake of dd1 after its translocation through the membrane and before further transfer to NirN, which catalyzes the last step of heme d_1 biosynthesis [18,22]. However, in this scenario it is not obvious why NirF is absolutely essential for heme d_1 formation. Alternatively, we therefore envisage a role of NirF as a biosynthetic enzyme, potentially involved in the introduction of the carbonyl functions at C3 and C8 of rings A and B to produce the heme d_1

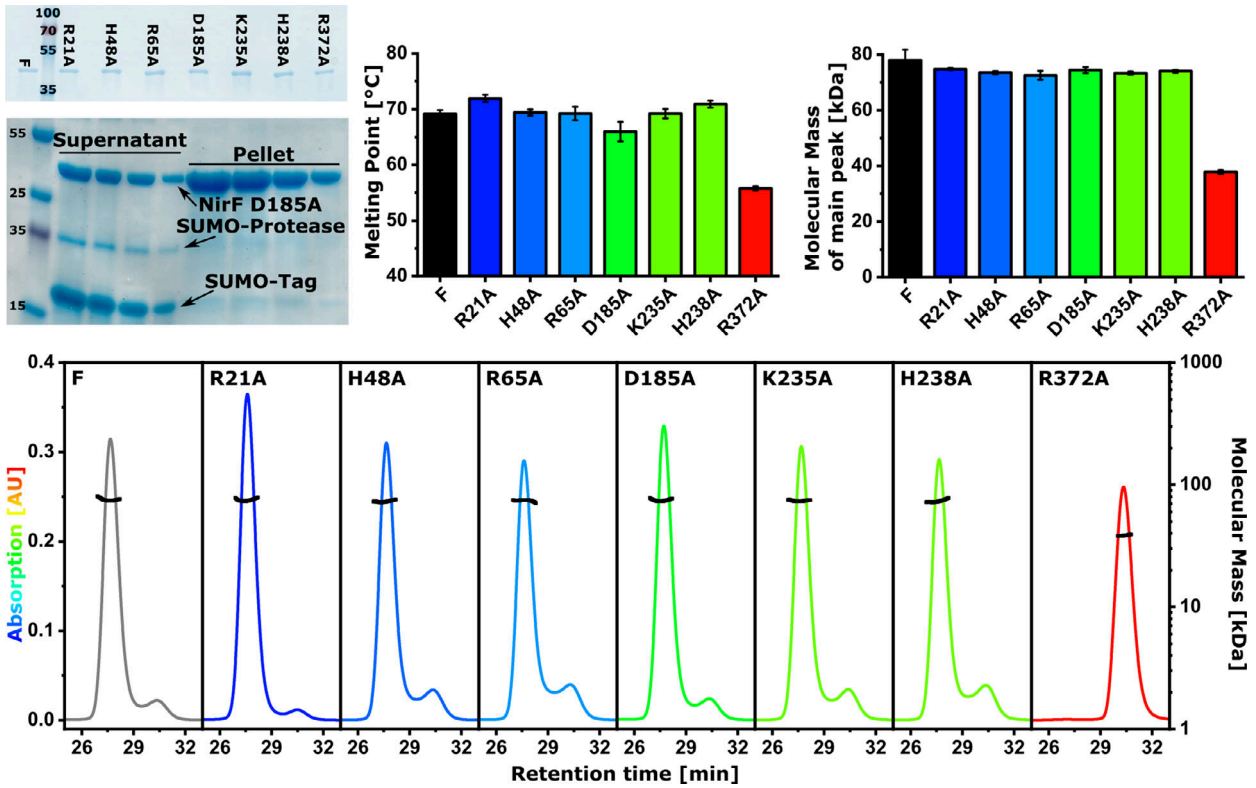

Fig. 9. SDS gels of the purified NirF wild-type (F) and mutant samples indicate high purity and similar size. The second SDS gel shows different dilutions of supernatant and pellet samples taken from NirF D185A after SUMO protease digestion and centrifugation. Bar diagrams show the melting points and molecular weight of NirF derivates determined by differential scanning fluorimetry and SEC-MALS measurements. Error bars represent standard deviations of triplicate measurements. In the bottom panel, representative SEC-MALS chromatograms are depicted with calculated molecular masses shown as black and UV absorption as colored lines.

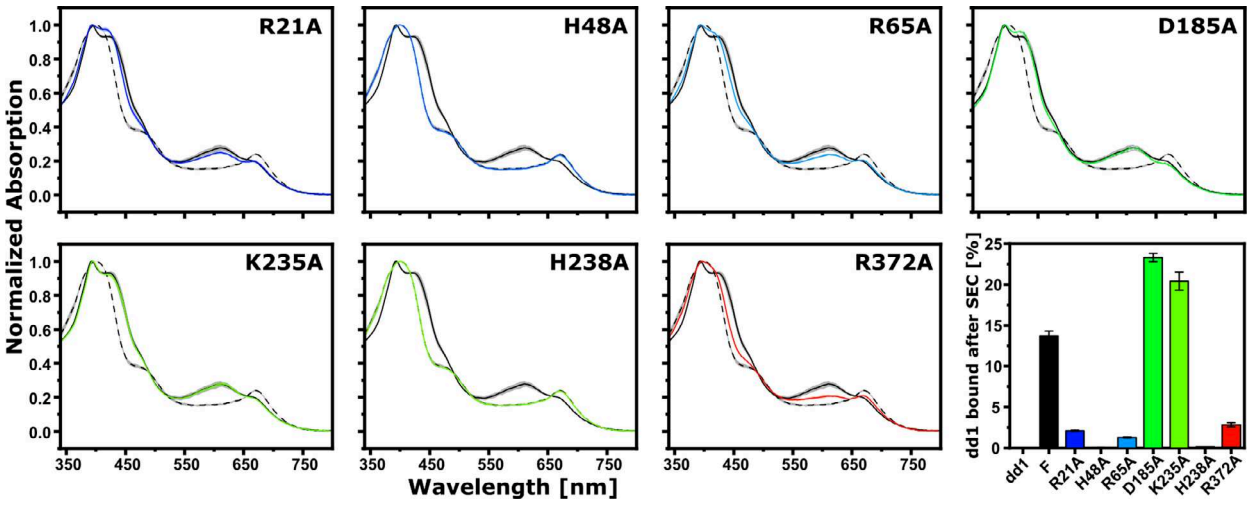

Fig. 10. Normalized, averaged, and smoothed UV/Vis spectra of dd1 binding to NirF variants. Black dashed lines represent spectra of dd1 not bound to NirF, solid black lines depict spectra of dd1 bound to wild-type NirF, and colored lines illustrate spectra of dd1 incubated with NirF variants. Gray/colored shadows represent the standard deviation (n = 3). The bar diagram depicts the amount of dd1 co-eluted with NirF after SEC after equimolar amounts were injected. Error bars indicate standard deviations (n = 3).

precursor dd1. The formation of these carbonyl groups is still enigmatic, and it has previously been speculated that they arise from oxidation by the radical SAM enzyme NirJ after this enzyme has removed the propionate groups of DDSH (Fig. 1) [17,31]. Since such a two-step oxidation by NirJ seems unlikely and has not been experimentally demonstrated, we hypothesize that the oxidation at C3 and C8 might be catalyzed by NirF instead. However, NirF would be an unusual oxidoreductase in that it does not possess a binding site for familiar redox cofactors such as NAD^+ or FAD [21] and would therefore require an alternative electron acceptor for enzymatic turnover. In this regard, it is interesting to note that the dehydrogenation reaction catalyzed by the structurally related NirN also does not rely on NAD^+ or FAD, but instead reduces its own cytochrome *c* moiety as well as the reaction product during catalysis. Since NirF does not possess a cytochrome *c* domain, an external redox-active protein could serve as such an electron acceptor here. This acceptor would possibly have to dock to NirF, and the outward-facing K235 might be involved in this interaction, providing a possible explanation for its requirement for denitrification in the cell-based experiments described above. The *nir*-operon of *P. aeruginosa* encodes two *c*-type cytochromes, NirC and NirM, and the role of NirC is not fully understood. Thus, we speculate that NirC might act as a redox partner of NirF in *P. aeruginosa*.

Conclusions

Previous studies have shown that NirF is required for heme d_1 biosynthesis [9,21]. Additionally, NirF was found to be periplasmic and, in certain bacteria such as the opportunistic pathogen *P. aeruginosa*, membrane-anchored via its N terminus [22]. Other components of the denitrification cascade interact with the protein; however, the exact role of NirF is still unclear [23]. Crystal structure analysis revealed that NirF adopts the predicted eight-bladed β-propeller fold and that the protein is homodimeric with an unusual bottom-to-bottom arrangement, which was confirmed by SAXS. Experiments with the monomeric variant R372A revealed, however, that dimerization is not essential for the unknown function of NirF, suggesting that it mainly contributes to the stabilization of the enzyme. This seems to resonate with the observation that the two binding sites for heme d_1 derivatives of the dimer locate opposite to the dimerization interface and are structurally independent of each other.

The NirF-dd1 complex structure revealed the position of the tetrapyrrole binding site as well as structural alterations that accompany dd1 binding. Several amino acid residues were identified that may be involved in the function of NirF. These residues were investigated for their importance in denitrification by *P. aeruginosa in vivo* and in dd1 binding *in vitro*. The strongest effect was observed for histidines H48 and H238, which are absolutely essential for *in vivo* function and *in vitro* tetrapyrrole binding. In contrast, NirF variants K235A and R65A were inactive *in vivo* despite binding dd1 *in vitro*. Together with data from the literature, this leads us to speculate that NirF represents a missing link in heme d_1 biosynthesis by acting as an oxidoreductase that produces the last known intermediate dd1 in an interplay with the monoheme cytochrome c NirC. We are currently devising experiments to test this hypothesis.

Materials and methods

Chemicals

All chemicals and media ingredients were purchased from Sigma-Aldrich (St. Louis, MO, USA) or from Carl Roth GmbH (Karlsruhe, Germany) unless stated otherwise.

Bacteria and plasmids

The bacterial strains and plasmids used in this study are listed in Tables S1 and S2. The *P. aeruginosa* strains PA01 RM301 (*nirF::tet*) [9] and RM361 (*nirN::tet*) [10] were a kind gift by H. Arai. The plasmid pUCP20T-*nirF* was from a previous study [22]. pMALX-E was provided by the Pedersen Lab [32], and pET-SUMO is a derivative of pET19 (Invitrogen, Carlsbad, CA, USA).

Construction of vectors

pUCP20T-*nirF* was used to PCR-amplify *nirF* without the N-terminal periplasmic export signal and the cysteine required for membrane anchoring. pET-SUMO and pMALX-E were digested with Nde1/BamHI or Nhe1/HindIII (New England Biolabs, Frankfurt, Germany), respectively. The PCR products were ligated with a QuickFusion Kit (Absource Diagnostics, Munich, Germany) and *E. coli* XL1-blue as a cloning host, resulting in plasmids pET-SUMO-*nirF* and pMALX-E-*nirF* encoding for the truncated *nirF* gene with an N-terminal 6xHis-SUMO- or MBP-tag. Site-directed mutagenesis of pUCP20T-*nirF* and pET-SUMO-*nirF* was performed by QuikChange mutagenesis. Primers used in this study are listed in Table S3. Prior to use, all plasmids were checked by Sanger sequencing using services provided by Eurofins (München, Germany) or SeqLab (Göttingen, Germany).

Transformation and bacterial cultures

Rubidium-competent *E. coli* cells were transformed by heat shock and selected on lysogeny broth (LB) agar (BD Bioscience, Franklin Lakes, NJ, USA) plates supplemented with 100 $\mu g \cdot mL^{-1}$ ampicillin [33]. *Pseudomonas aeruginosa* strains were transformed by electroporation using a Gene Pulser II (Bio-Rad, Hercules, CA, USA) and selected on LB agar plates supplemented with 250 $\mu g \cdot mL^{-1}$ carbenicillin [34]. Overnight cultures were started by inoculating LB media containing the required antibiotics with single colonies. The production of SUMO-NirF and MALX-E-NirF in *E. coli* BL21 was performed in 1 L auto-induction media [35]. Cultures were incubated for 4 h at 37 °C before the temperature was reduced to 20 °C, and growth was continued for another 12–16 h. For the production of dd1, *P. aeruginosa* PA01 RM361 was grown under denitrifying conditions as previously described [18,26]. Cells were harvested by centrifugation, frozen in liquid nitrogen, and stored at −20 °C until needed.

Pseudomonas aeruginosa growth curves and nitrite/nitrate determination

Aerobically grown overnight cultures of *P. aeruginosa* were used to inoculate a modified AB minimal medium [36] supplemented with 75 mM $NaNO_3$, 200 μM 5-aminolevulinic acid (Alfa Aesar, Haverhill, MA, USA), 200 μM $Fe(II)SO_4$, and 250 μM carbenicillin to an optical density of ~ 0.005. Two-hundred microliter of culture was filled in honeycomb plates and overlaid with 200 μL of paraffin oil to prevent O_2 exchange with the air. Growth at 37 °C was monitored in a Bioscreen C instrument (Oy Growth Curves Ab Ltd, Helsinki, Finland). After 24 h, the cultures were harvested and centrifuged in a table-top centrifuge. Nitrite and nitrate concentrations of the supernatant were determined using a colorimetric assay kit (Cayman Chemicals, Ann Arbor, MI, USA). For each strain, growth curves of four biological replicates with three technical replicates for each were collected. For some technical replicates, bubbles started to accumulate after ~ 12 h between oil and culture, leading to discontinuous growth curves. These cultures were excluded from the analysis, if the effect already occurred before the 12-h mark. The remaining technical replicates were averaged to give the growth curve of one biological replicate. The average of all four biological replicates was then produced for the final analysis.

Purification of recombinant NirF

Purification of MALX-E-NirF and SUMO-NirF was conducted in a buffer consisting of 10 mM Tris pH 8.0, 500 mM NaCl, and 10 % (v/v) glycerol (protein buffer). *Escherichia coli* cell pellets were resuspended in protein buffer containing cOmplete Protease Inhibitor Cocktail (Roche, Basel, Switzerland), lysed by sonication, and centrifuged for 45 min at 38 000 ***g*** to remove cell debris. All further steps were performed at room temperature since NirF derivatives were found to be less soluble at low temperature (see main text). To purify SUMO-NirF and its variants, the cleared lysate was loaded onto a 5 mL HisTrap FF column (GE Healthcare, Chicago, IL, USA) connected to an Äkta Purifier FPLC System (GE Healthcare). The column was washed with three column volumes of protein buffer supplemented with 20 mM imidazole before elution with a gradient to 250 mM imidazole. The SUMO-tag was then removed with 6xHis-tagged SUMO-protease in the course of overnight dialysis against protein buffer containing 1 mM of DTT. To separate the cleaved tag and the protease, NirF was again loaded onto the 5 mL HisTrap FF column and eluted with a gradient to 50 mM imidazole. MALX-E-NirF was purified by loading the cleared cell lysate onto a 5 m: MBPTrap HP column (GE Healthcare) which was eluted with a gradient to 20 mM maltose. The MBP-tag was not removed for subsequent experiments. All proteins were further purified by SEC using a HiLoad 26/60 Superdex 200 pg column (GE Healthcare). The purity of proteins was confirmed with SDS/PAGE and concentrations were determined photometrically, using a NanoDrop 2000 (Thermo Fisher Scientific, Waltham, MA, USA) with extinction coefficients calculated by PROTPARAM [37]. The identity of the isolated proteins and presence of assigned amino acid exchanges were checked by mass spectrometry.

Purification of dihydroheme d_1

Dihydroheme d_1 was obtained by solvent extraction from purified NirS from *P. aeruginosa* PA01 RM361 using acidified ethyl acetate as described by Adamczack *et al.* [18]. Concentrations of dd1 in solution were determined with extinction coefficients published previously [26].

Crystallization of NirF

Crystallization experiments were set up with a HoneyBee 961 robot (Digilab Genomic Solutions, Hopkinton, MA, USA) mixing 200 nL of reservoir with 200 nL of protein solution equilibrated against 60 μL of reservoir in 96-well sitting-drop vapor diffusion plates (Intelli 96-3 plates, Art Robbins Instruments, Sunnyvale, CA, USA). Initial crystallization conditions were identified with commercial sparse matrix screens JCSG+ (Qiagen, Hilden, Germany), Index (Hampton Research, Aliso Viejo, CA, USA), Morpheus (Molecular Dimension, Newmarket, UK), and polyethylene glycol (PEG) Suite (Qiagen). Diffracting crystals of the MALX-E-NirF fusion protein were obtained with 30 $mg \cdot mL^{-1}$ protein and a precipitant containing 20% (w/v) polyethylene glycol 3350 and 0.2 M ammonium formate. Crystals of free NirF, purified from the SUMO-NirF fusion

protein, were obtained with several precipitants, but only those containing polyethylene glycol 3350 or polyethylene glycol 4000 gave crystals that diffracted X-rays. Optimizing these conditions yielded crystals of similar quality but never surpassed one directly fished from the Morpheus screen. Presented data are from crystals grown in Morpheus condition C7 and H7 as described by Gorrec *et al.* [38] using protein concentration of 5 mg·mL^{-1} or 10 mg·mL^{-1}. A complex with dd1 was obtained by soaking in ligand-saturated mother liquor for 1 day. Cryoprotection was achieved by washing in reservoir solution containing 10% of (*R*,*R*)-2,3-butanediol (Alfa Aesar) for a few minutes prior to flash-cooling in liquid nitrogen.

Data collection and processing

Two thousand to three thousand six hundred diffraction images per crystal were collected at the beamline P11 at PETRA III (DESY, Hamburg, Germany) [39] on a PILATUS 6M fast detector with an oscillation angle of 0.1° per images. Reflections were indexed and integrated with DIALS [40]. Integrated reflections were further processed with POINTLESS [41] and AIMLESS [42]. As the datasets of NirF crystals showed strong anisotropy, they were truncated with a local $I/\sigma(I)$ of 1.2 and corrected using the STARANISO server [25]. Quality of data was assessed using XTRIAGE confirming the presence of tNCS in all datasets [24]. Processing and data quality statistics can be found in Table S1.

Structure determination and refinement

Initial phases were first obtained for the low-resolution diffraction data of the MALX-E-NirF fusion protein, using molecular replacement in PHASER [43]. Search models consisted of a crystal structure of MBP (PDB: 4QVH [44]) and an ensemble of the heme d_1 binding domains of NirN (PDB: 6RTE [26]) and NirS (PDB: 1NNO [45]). Based on the resulting electron density, the search model for the heme d_1 binding domains was truncated containing to ~ 80% of all residues. This modified model was then sufficient for molecular replacement in the diffraction data obtained from crystals of the untagged protein. Structures were subsequently refined by manual adjustments in COOT [46] and computational optimization in REFMAC5 [47] of the CCP4 suite [48] and PHENIX.REFINE [49] of the PHENIX suite [50], applying TLS refinement [51] in the last steps of the procedure. Dihydroheme d_1 was placed in the $|F_O\text{-}F_C|$ difference electron density appearing if the crystals were soaked. For a first estimate of the ligand occupancy, an anomalous map of the iron signal was calculated with ANODE [52]. After refinement with fixed occupancies, the average B-factors of the ligand were compared to those of the surrounding protein chains and the occupancies were then adjusted in 0.05 steps until the average B-factors were similar, resulting in occupancies between 75% and 100%. Depictions of the models were made using the PYMOL molecular graphics system (Schrödinger LLC; version 2.3.2). Model and refinement statistics are summarized in Table 1. The structures can be accessed under the PDB codes 6TV2 and 6TV9.

Small-angle X-ray scattering

Small-angle X-ray scattering experiments were performed at beamline BM29 BioSAXS of the European Synchrotron Radiation Facility (ESRF, Grenoble, France) [53] on a PILATUS 1M detector. Scattering data were measured online after 150 or 450 µg NirF were separated on a 10/300 Superdex 200 increase size-exclusion column utilizing protein buffer without glycerol. Data processing and bead model calculation were performed with the ATSAS software package (version 2.8.4 [54]). Theoretical SAXS profiles of PDB models were calculated with the FoXS Server [55]. The side-by-side homodimer model of NirF shown in Fig. 3 was generated by superposing NirF monomers onto the NirS homodimer (PDB: 1nir [5]).

Size-exclusion chromatography with multi-angle light scattering

Size-exclusion chromatography with MALS (SEC-MALS) was used to determine particle sizes in solution. A 10/300 Superdex 200 increase column (GE Healthcare) equilibrated in protein buffer was coupled to an Agilent Technologies 1260 Infinity II HPLC System (Santa Clara, CA, USA) equipped with a Wyatt Optilab rEX diffraction index detector and a TREOS II multi-angle laser light scattering detector (Wyatt, Santa Barbara, CA, USA). Data were processed with ASTRA (7.3.0) utilizing a cratio of 0.185 mL·g^{-1}. Measurements were performed in triplicates.

Determination of melting temperatures

Protein melting temperatures were determined by difference scanning fluorimetry utilizing the intrinsic fluorescence of tryptophan and tyrosine measured in a Tycho NT6 System (NanoTemper, Munich, Germany). Results are average of three independent measurements with two technical replicates for each measurement.

Dihydroheme d_1 binding studies

Binding of dd1 to *P. aeruginosa* NirF was assessed with two UV/Vis-based methods. Because spectral features associated with binding were found to be more pronounced at lower pH, the protein was rebuffered to 50 mM Bis-Tris pH 6.5, 500 mM NaCl, and 10% (v/v) glycerol using Zeba spin columns (Thermo Fisher Scientific). First, 30 µL of

solutions at 40 μM of dd1 and 40 μM NirF were subjected to SEC using the setup described for MALS experiments, albeit with a 5/150 Superdex 75 increase column (GE Healthcare). Elution was followed by measuring the absorption at 395 nm. The area under the curve for co-eluted dd1 was calculated and normalized against the complete signal. Second, remaining samples were diluted to 5 μM and UV/Vis spectra were recorded between 340 and 800 nm using an Evolution Bio 260 UV/Vis Spectrophotometer (Thermo Fisher Scientific). The spectra shown in Fig. 10 were normalized, averaged, and smoothed (Savitzky–Golay algorithm). These experiments were performed three times, including controls without protein or dd1 in the sample.

Acknowledgements

We thank the beamline staff at P11 at the PETRA III synchrotron (Deutsches Elektronen-Synchrotron DESY, Hamburg, Germany) and at BM29 (European Synchrotron Radiation Facility ESRF, Grenoble, France) for letting us use their facilities. We acknowledge Alejandro Arce Rodriguez and Susanne Häußler for their support in collecting growth curves of the *P. aeruginosa* strains and Sabrina Hafke for support during protein purification. This work was supported by grants from the Deutsche Forschungsgemeinschaft to GL (LA 2412/3-2) and WB (PROCOMPAS graduate school, GRK 2223/1).

Conflicts of interest

The authors declare no conflict of interest.

Author contributions

TK and WB designed the experiments. TK and MN performed the experiments. TK, MN, LJ, and WB interpreted the data. TK, GL, and WB wrote and edited the manuscript. All authors carefully revised the manuscript.

References

1 Zumft WG (1997) Cell biology and molecular basis of denitrification. *Microbiol Mol Biol Rev* **61**, 533–616.
2 Sønderholm M, Bjarnsholt T, Alhede M, Kolpen M, Jensen PØ, Kühl M & Kragh KN (2017) The consequences of being in an infectious biofilm. Microenvironmental conditions governing antibiotic tolerance. *Int J Mol Sci* **18**, 2688.
3 Yamanaka T, Ota A & Okunuki K (1961) A nitrite reducing system reconstructed with purified cytochrome components of *Pseudomonas aeruginosa*. *Biochem Biophys Acta* **53**, 294–308.
4 Cutruzzolà F, Rinaldo S, Centola F & Brunori M (2003) NO production by *Pseudomonas aeruginosa* cd1 nitrite reductase. *IUBMB Life* **55**, 617–621.
5 Nurizzo D, Silvestrini M-C, Mathieu M, Cutruzzolà F, Bourgeois D, Fülöp V, Hajdu J, Brunori M, Tegoni M & Cambillau C (1997) N-terminal arm exchange is observed in the 2.15 Å crystal structure of oxidized nitrite reductase from *Pseudomonas aeruginosa*. *Structure* **5**, 1157–1171.
6 Farver O, Brunori M, Cutruzzolà F, Rinaldo S, Wherland S & Pecht I (2009) Intramolecular electron transfer in *Pseudomonas aeruginosa* cd(1) nitrite reductase: thermodynamics and kinetics. *Biophys J* **96**, 2849–2856.
7 Chang CK (1985) On the structure of heme d1. An isobacteriochlorin derivative as the prosthetic group of dissimilatory nitrite reductase? *J Biol Chem* **260**, 9520–9522.
8 Chang CK, Timkovich R & Wu W (1986) Evidence that heme d1 is a 1,3-porphyrindione. *Biochemistry* **25**, 8447–8453.
9 Kawasaki S, Arai H, Igarashi Y & Kodama T (1995) Sequencing and characterization of the downstream region of the genes encoding nitrite reductase and cytochrome c-551 (nirSM) from *Pseudomonas aeruginosa*: identification of the gene necessary for biosynthesis of heme d1. *Gene* **167**, 87–91.
10 Kawasaki S, Arai H, Kodama T & Igarashi Y (1997) Gene cluster for dissimilatory nitrite reductase (nir) from *Pseudomonas aeruginosa*: sequencing and identification of a locus for heme d1 biosynthesis. *J Bacteriol* **179**, 235–242.
11 Bali S, Palmer DJ, Schroeder S, Ferguson SJ & Warren MJ (2014) Recent advances in the biosynthesis of modified tetrapyrroles: the discovery of an alternative pathway for the formation of heme and heme d 1. *Cell Mol Life Sci* **71**, 2837–2863.
12 Ohshima T, Sugiyama M, Uozumi N, Iijima S & Kobayashi T (1993) Cloning and sequencing of a gene encoding nitrite reductase from *Paracoccus denitrificans* and expression of the gene in *Escherichia coli*. *J Ferment Bioeng* **76**, 82–88.
13 Zajicek RS, Bali S, Arnold S, Brindley AA, Warren MJ & Ferguson SJ (2009) d(1) haem biogenesis - assessing the roles of three nir gene products. *FEBS J* **276**, 6399–6411.
14 Storbeck S, Walther J, Müller J, Parmar V, Schiebel HM, Kemken D, Dülcks T, Warren MJ & Layer G (2009) The *Pseudomonas aeruginosa* nirE gene encodes the S-adenosyl-L-methionine-dependent uroporphyrinogen III methyltransferase required for heme d(1) biosynthesis. *FEBS J* **276**, 5973–5982.

15 Warren MJ, Bolt EL, Roessner CA, Scott AI, Spencer JB & Woodcock SC (1994) Gene dissection demonstrates that the *Escherichia coli* cysG gene encodes a multifunctional protein. *Biochem J* **302**, 837–844.
16 Bali S, Lawrence AD, Lobo SA, Saraiva LM, Golding BT, Palmer DJ, Howard MJ, Ferguson SJ & Warren MJ (2011) Molecular hijacking of siroheme for the synthesis of heme and d1 heme. *Proc Natl Acad Sci USA* **108**, 18260–18265
17 Boss L, Oehme R, Billig S, Birkemeyer C & Layer G (2017) The radical SAM enzyme NirJ catalyzes the removal of two propionate side chains during heme d1 biosynthesis. *FEBS J* **284**, 4314–4327.
18 Adamczack J, Hoffmann M, Papke U, Haufschildt K, Nicke T, Bröring M, Sezer M, Weimar R, Kuhlmann U, Hildebrandt P *et al.* (2014) NirN protein from *Pseudomonas aeruginosa* is a novel electron-bifurcating dehydrogenase catalyzing the last step of heme d1 biosynthesis. *J Biol Chem* **289**, 30753–30762.
19 de Boer Anthonius P N, Reijnders WNM, Kuenen JG, Stouthamer AH & van Spanning Rob J M (1994) Isolation, sequencing and mutational analysis of a gene cluster involved in nitrite reduction in *Paracoccus denitrificans*. *Antonie Van Leeuwenhoek* **66**, 111–127.
20 Palmedo G, Seither P, Körner H, Matthews JC, Burkhalter RS, Timkovich R & Zumft WG (1995) Resolution of the nirD Locus for Heme d1, synthesis of cytochrome cd1, (respiratory nitrite reductase) from *Pseudomonas Stutzeri*. *Eur J Biochem* **232**, 737–746.
21 Bali S, Warren MJ & Ferguson SJ (2010) NirF is a periplasmic protein that binds d1 heme as part of its essential role in d1 heme biogenesis. *FEBS J* **277**, 4944–4955.
22 Nicke T, Schnitzer T, Münch K, Adamczack J, Haufschildt K, Buchmeier S, Kucklick M, Felgenträger U, Jänsch L, Riedel K *et al.* (2013) Maturation of the cytochrome cd1 nitrite reductase NirS from *Pseudomonas aeruginosa* requires transient interactions between the three proteins NirS, NirN and NirF. *Biosci Rep* **33**, e00048.
23 Borrero-de Acuña JM, Rohde M, Wissing J, Jänsch L, Schobert M, Molinari G, Timmis KN, Jahn M & Jahn D (2016) Protein network of the *Pseudomonas aeruginosa* denitrification apparatus. *J Bacteriol* **198**, 1401–1413.
24 Zwart PH, Grosse-Kunstleve RW & Adams PD (2005) Xtriage and Fest: automatic assessment of X-ray data and substructure structure factor estimation. CCP4 Newsletter 43. http://www.ccp4.ac.uk/newsletters/newsletter43/articles/PHZ_RWGK_PDA.pdf
25 Tickle IJ, Flensburg C, Keller P, Paciorek W, Sharff A, Vonrhein C & Bricogne G (2018) STARANISO. Cambridge. http://staraniso.globalphasing.org/cgi-bin/staraniso.cgi
26 Klünemann T, Preuß A, Adamczack J, Rosa LFM, Harnisch F, Layer G & Blankenfeldt W (2019) Crystal structure of dihydro-heme d1 dehydrogenase NirN from *Pseudomonas aeruginosa* reveals amino acid residues essential for catalysis. *J Mol Biol* **431**, 3246–3260.
27 Krissinel E & Henrick K (2007) Inference of macromolecular assemblies from crystalline state. *J Mol Biol* **372**, 774–797.
28 Fülöp V, Moir JWB, Ferguson SJ & Hajdu J (1995) The anatomy of a bifunctional enzyme: structural basis for reduction of oxygen to water and synthesis of nitric oxide by cytochrome cd1. *Cell* **81**, 369–377.
29 Berka K, Hanák O, Sehnal D, Banáš P, Navrátilová V, Jaiswal D, Ionescu C-M, Svobodová Vareková R, Koca J & Otyepka M (2012) MOLEonline 2.0: interactive web-based analysis of biomacromolecular channels. *Nucleic Acids Res* **40**, W222–W227.
30 Neet KE & Timm DE (1994) Conformational stability of dimeric proteins: quantitative studies by equilibrium denaturation. *Protein Sci* **3**, 2167–2174.
31 Brindley AA, Zajicek R, Warren MJ, Ferguson SJ & Rigby SEJ (2010) NirJ, a radical SAM family member of the d1 heme biogenesis cluster. *FEBS Lett* **584**, 2461–2466.
32 Moon AF, Mueller GA, Zhong X & Pedersen LC (2010) A synergistic approach to protein crystallization: combination of a fixed-arm carrier with surface entropy reduction. *Protein Sci* **19**, 901–913.
33 Green R & Rogers EJ (2013) Transformation of chemically competent *E. coli*. *Methods Enzymol* **529**, 329–336.
34 Enderle PJ & Farwell MA (1998) Electroporation of freshly plated *Escherichia coli* and *Pseudomonas aeruginosa* cells. *Biotechniques* **25**, 954–956, 958.
35 Studier FW (2005) Protein production by auto-induction in high-density shaking cultures. *Protein Expr Purif* **41**, 207–234.
36 Heydorn A, Nielsen AT, Hentzer M, Sternberg C, Givskov M, Ersbøll BK & Molin S (2000) Quantification of biofilm structures by the novel computer program COMSTAT. *Microbiology (Reading, England)* **146** (Pt 10), 2395–2407.
37 Gasteiger E, Hoogland C, Gattiker A, Duvaud S, Wilkins MR, Appel RD & Bairoch A. Protein identification and analysis tools on the ExPASy Server. In Proteomics Protocols Handbook (Walker JM ed), pp. 571–607. Humana Press, Totowa, NJ.
38 Gorrec F (2009) The MORPHEUS protein crystallization screen. *J Appl Crystallogr* **42**, 1035–1042.
39 Burkhardt A, Pakendorf T, Reime B, Meyer J, Fischer P, Stübe N, Panneerselvam S, Lorbeer O, Stachnik K, Warmer M *et al.* (2016) Status of the crystallography beamlines at PETRA III. *Eur Phys J Plus* **131**, 25.
40 Winter G, Waterman DG, Parkhurst JM, Brewster AS, Gildea RJ, Gerstel M, Fuentes-Montero L, Vollmar M,

Michels-Clark T, Young ID *et al.* (2018) DIALS: implementation and evaluation of a new integration package. *Acta Crystallogr D* **74**, 85–97.
41 Evans PR (2011) An introduction to data reduction: space-group determination, scaling and intensity statistics. *Acta Crystallogr D* **67**, 282–292.
42 Evans PR & Murshudov GN (2013) How good are my data and what is the resolution? *Acta Crystallogr D* **69**, 1204–1214.
43 McCoy AJ, Grosse-Kunstleve RW, Adams PD, Winn MD, Storoni LC & Read RJ (2007) Phaser crystallographic software. *J Appl Crystallogr* **40**, 658–674.
44 Jung J, Bashiri G, Johnston JM, Brown AS, Ackerley DF & Baker EN (2014) Crystal structure of the essential *Mycobacterium tuberculosis* phosphopantetheinyl transferase PptT, solved as a fusion protein with maltose binding protein. *J Struct Biol* **188**, 274–278.
45 Nurizzo D, Cutruzzolà F, Arese M, Bourgeois D, Brunori M, Cambillau C & Tegoni M (1998) Conformational changes occurring upon reduction and NO binding in nitrite reductase from *Pseudomonas aeruginosa*. *Biochemistry* **37**, 13987–13996.
46 Emsley P, Lohkamp B, Scott WG & Cowtan K (2010) Features and development of Coot. *Acta Crystallogr D* **66**, 486–501.
47 Murshudov GN, Skubák P, Lebedev AA, Pannu NS, Steiner RA, Nicholls RA, Winn MD, Long F & Vagin AA (2011) REFMAC5 for the refinement of macromolecular crystal structures. *Acta Crystallogr D* **67**, 355–367.
48 Winn MD, Ballard CC, Cowtan KD, Dodson EJ, Emsley P, Evans PR, Keegan RM, Krissinel EB, Leslie AGW, McCoy A *et al.* (2011) Overview of the CCP4 suite and current developments. *Acta Crystallogr D* **67**, 235–242.
49 Afonine PV, Grosse-Kunstleve RW, Echols N, Headd JJ, Moriarty NW, Mustyakimov M, Terwilliger TC, Urzhumtsev A, Zwart PH & Adams PD (2012) Towards automated crystallographic structure refinement with phenix.refine. *Acta Crystallogr D* **68**, 352–367.
50 Adams PD, Afonine PV, Bunkóczi G, Chen VB, Davis IW, Echols N, Headd JJ, Hung L-W, Kapral GJ, Grosse-Kunstleve RW *et al.* (2010) PHENIX: a comprehensive Python-based system for macromolecular structure solution. *Acta Crystallogr D* **66**, 213–221.
51 Schomaker V & Trueblood KN (1968) On the rigid-body motion of molecules in crystals. *Acta Crystallogr B* **24**, 63–76.
52 Thorn A & Sheldrick GM (2011) ANODE: anomalous and heavy-atom density calculation. *J Appl Crystallogr* **44**, 1285–1287.
53 Pernot P, Round A, Barrett R, de Maria Antolinos A, Gobbo A, Gordon E, Huet J, Kieffer J, Lentini M, Mattenet M *et al.* (2013) Upgraded ESRF BM29 beamline for SAXS on macromolecules in solution. *J Synchrotron Radiat* **20**, 660–664.
54 Franke D, Petoukhov MV, Konarev PV, Panjkovich A, Tuukkanen A, Mertens HDT, Kikhney AG, Hajizadeh NR, Franklin JM, Jeffries CM *et al.* (2017) ATSAS 2.8: a comprehensive data analysis suite for small-angle scattering from macromolecular solutions. *J Appl Crystallogr* **50**, 1212–1225.
55 Schneidman-Duhovny D, Hammel M, Tainer JA & Sali A (2013) Accurate SAXS profile computation and its assessment by contrast variation experiments. *Biophys J* **105**, 962–974.
56 Davis IW, Leaver-Fay A, Chen VB, Block JN, Kapral GJ, Wang X, Murray LW, Arendall WB, Snoeyink J, Richardson JS *et al.* (2007) MolProbity: all-atom contacts and structure validation for proteins and nucleic acids. *Nucleic Acids Res* **35**, W375–W383.
57 Jurrus E, Engel D, Star K, Monson K, Brandi J, Felberg LE, Brookes DH, Wilson L, Chen J, Liles K *et al.* (2018) Improvements to the APBS biomolecular solvation software suite. *Protein Sci* **27**, 112–128.
58 Sievers F, Wilm A, Dineen D, Gibson TJ, Karplus K, Li W, Lopez R, McWilliam H, Remmert M, Söding J *et al.* (2011) Fast, scalable generation of high-quality protein multiple sequence alignments using Clustal Omega. *Mol Syst Biol* **7**, 539.
59 Robert X & Gouet P (2014) Deciphering key features in protein structures with the new ENDscript server. *Nucleic Acids Res* **42**, W320–W324.

Supporting information

Additional supporting information may be found online in the Supporting Information section at the end of the article.

Table S1. Plasmids used in this work.

Table S2. Strains used in this work.

Table S3. Primers used in this work.